J. Phys. Chem. A **2002,** *106,* 10543−10549

The Nucleation and Freezing of Dilute Nitric Acid Aerosols

D. B. Dickens and J. J. Sloan*

Department of Chemistry, University of Waterloo, Waterloo, Ontario N2L 3G1, Canada

Received: April 16, 2002; In Final Form: September 3, 2002

We report the kinetically constrained phase diagram for nitric acid−water aerosols over the range of nitric acid mole fractions from 0 to 0.5, measured using a temperature-programmable cryogenic flow tube. The freezing temperatures of the aerosol particles, which have radii on the order of 1 μm, are 30−90 K lower than those of the bulk, and the liquid−solid phase boundaries are modified by the differences in the activation energies for nucleation of the nitric acid hydrates. We infer from the shapes of the respective supersaturation curves that water ice nucleates in the liquid droplets at nitric acid mole fractions below about 0.15, and nitric acid trihydrate grows on these ice nuclei. At higher concentrations, nitric acid dihydrate crystals nucleate, and either ice or nitric acid trihydrate crystals grow on the nuclei. Using realistic estimates of the nucleation rate constants, we conclude that ice will nucleate homogeneously in upper tropospheric clouds having nitric acid mole fractions as high as 0.1 if the temperature decreases to 210 K.

Introduction

When temperatures in the winter polar stratosphere fall below about 194 K, stratospheric sulfate aerosols take up water and nitric acid vapor until the relative concentration of sulfuric acid becomes nearly negligible and the particles approach the composition of binary HNO_3−H_2O solutions.[1−6] The resulting aerosols have many of the optical characteristics of type 1 polar stratospheric clouds (PSCs), which consist of pure binary nitric acid aerosols. These have been studied for many years[7,8] using remote sensing measurements such as lidar[9] and balloon-borne sondes.[10]

Nitric acid is also present in the upper troposphere at concentrations of a few parts per billion by volume (ppbv),[11] and at typical upper tropospheric temperatures and relative humidities, dilute nitric acid aerosols exist in equilibrium with this gas-phase HNO_3.[12;13] Cirrus and subvisible cirrus clouds with optical properties similar to type 1a PSCs have been observed near the equatorial tropopause at temperatures ranging from 185 to 200 K,[14] and increasing nitric acid pollution in the upper troposphere increases both the concentration of HNO_3 in these particles and their number density.[15] The phase (solid or liquid) of these stratospheric and upper tropospheric clouds affects climate (via the cloud reflectivity) and ozone depletion,[16] so it is important to know the freezing points of these dilute nitric acid aerosols accurately.

More than forty laboratory studies on phase changes in stratospheric aerosol particles have been reported during the past 10 years, and more than half of these focus on type 1 PSCs. Recent publications have reported the freezing of binary H_2O/HNO_3 particles having nitric acid mole fractions ($x\mathrm{HNO_3}$) in the range $0.16 \leq x\mathrm{HNO_3} \leq 0.46$.[17−21] As a result of this work, it is known that the presence of HNO_3 changes the low-temperature behavior of the particles significantly from that of bulk solutions. For example, the low-temperature nucleation rate of nitric acid dihydrate (NAD) exceeds that of the trihydrate (NAT) by up to 4 orders of magnitude over the composition range of approximately $0.25 \leq x\mathrm{HNO_3} \leq 0.42$, despite the fact that NAT is thermodynamically more stable. Furthermore, in the aerosol, the nucleation temperature decreases with decreasing nitric acid concentration in the range $0.25 < x\mathrm{HNO_3} < 0.33$, whereas for bulk solutions it increases in this concentration range. These differences are caused by the kinetics of homogeneous nucleation in the aerosol droplets—a subject that is beginning to be explored by theory but as yet is only poorly understood at a fundamental level. Thus, direct measurements of cloud droplet freezing temperatures are required to provide information for stratospheric and upper tropospheric modeling.

In the present work, we extend our previous measurements on binary HNO_3−H_2O aerosols to dilute particles having compositions in the range $0 \leq x\mathrm{HNO_3} \leq 0.25$. This composition range is most important in lower stratospheric and upper tropospheric clouds. As in the previous work, we identify both the temperature at which nucleation occurs and also the first crystalline substance that is formed. These measurements complete our study of the kinetic phase diagram over the range $0 \leq x\mathrm{HNO_3} \leq 0.5$.

Freezing temperatures for binary nitric acid aerosol droplets in part of this concentration range, from 0 to 33 wt % ($0 \leq x\mathrm{HNO_3} \leq 0.12$), have been measured previously using differential scanning calorimetry on micrometer-sized droplets dispersed in an inert oil matrix.[22] Our results agree with this earlier work for very dilute aerosol droplets, but in the range $0.16 \leq x\mathrm{HNO_3} \leq 0.38$, they disagree. We find that crystalline NAT and NAD are formed in this higher concentration range, whereas the differential scanning calorimetry results suggest glass formation. We are not able to suggest a reason for this difference at the present time.

Measurements

The measurement is designed to determine the temperature at which crystalline material nucleates from micron-sized nitric acid aerosol particles of known composition and to identify the crystals that form. The apparatus that we use for these measurements, which has been described previously,[19] consists of a cryogenic flow tube having optical ports through which FTIR spectra of the aerosol are recorded. The flow tube is composed of three copper sections (8.5 cm inside diameter, i.d.), which are thermally isolated from each other by thin-walled

10.1021/jp0259566 CCC: \$22.00

stainless steel bellows, also 8.5 cm i.d. The tube is temperature-programmable; each section can be independently cooled to a minimum temperature near 120 K. A maximum temperature difference of about 100 K can be sustained between adjacent sections. The tube is operated in a vertical position with the warmer (inlet) section at the top to minimize convection. The axial temperature profile is monitored using 10 copper/constantan (type T) thermocouples located on the walls: three in the top section, three in the middle section, and four in the lowest (observation) section. Using a thermocouple mounted on a thin probe that could be moved axially down the tube, we have determined that the maximum difference in operating temperature between the center axis and the walls of any section is less than the combined thermocouple uncertainty of 1.6 K.

The total pressure was maintained at 1000 mbar using nitrogen carrier gas to minimize the diffusion of water vapor to the walls, which changes the concentration of the aerosol droplets. The total gas flow rate was 5 standard L/min, giving a residence time of about 18 s in the first section, 21−36 s in the second section and 53−75 s in the bottom section. The ranges in residence times result from variations in the carrier gas density at the temperatures of the different experiments. In the following, we will refer to the second and third sections as the nucleation and observation sections, respectively.

Nitric acid aerosols were generated from a nitric acid solution using an ultrasonic nebulizer and transported by a nitrogen carrier gas into the top section of the flow tube. Depending on the flow rates and operating parameters of the nebulizer, the droplets had mean radii between 0.7 and 2 μm. The aerosol is cooled to approximately 240 K in the top section of the flow tube. The particle size and concentration change slightly because of loss of material to the walls during the cooling process, but there is very little loss of material after the inlet section because vapor phase diffusion is negligible at the low temperatures and high pressures of the experiments. The final size distribution and composition of the particles are determined in the observation section, using a procedure to be described below.

Typically, an experiment begins with the temperature of the middle (nucleation) section below 150 K. At this temperature, nuclei form in all liquid droplets, and all particles have crystallized by the time they reach the observation section. The nucleation section temperature is then scanned upward slowly, while recording spectra in the bottom (observation) section. The temperature in the observation section is held about 20 K above that in the nucleation section to cause any nuclei that are formed to grow rapidly into crystals that are large enough to be detected. FTIR spectra are recorded at the bottom of the observation section using a single pass configuration in which the optical axis of the FTIR spectrometer is perpendicular to the flow axis, thus ensuring that all particles are observed after the same residence time. These IR spectra not only detect the solid crystals, of course, but also identify the crystalline compound that forms.

Determination of Concentrations. The compositions of the cold droplets were determined from their FTIR spectra. This information is obtained from spectra measured when the droplets were close to, but slightly above, their nucleation temperature. The intensities of the NO_3^- and H_3O^+ bands in the region between about 1250 and 1700 cm^{-1} were used for this purpose. The basis for the use of the NO_3^- band is the fact that in pure (24 M) liquid nitric acid, the ν_3(E) mode of NO_3^- is doubly degenerate and its spectrum consists of a single band between 1210 and 1460 cm^{-1}. When water is present and the acid becomes partly hydrolyzed, this degeneracy is split and the ν_3(E) band becomes a doublet.[23] The shape of this doublet and the intensities of its components depend on the concentration.

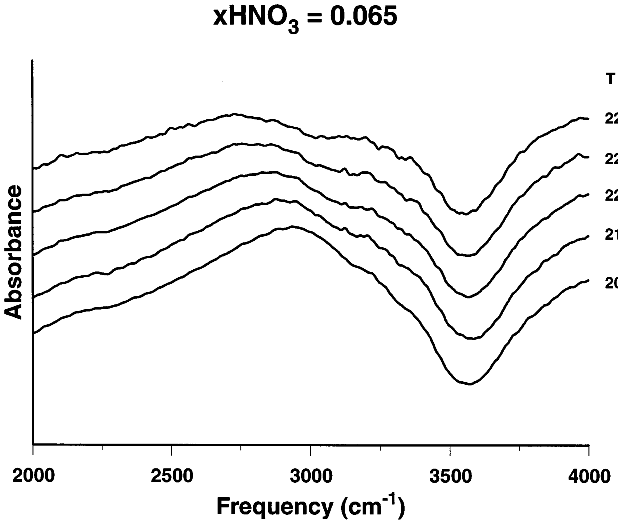

Figure 1. Temperature dependence of the spectra of dilute nitric acid droplets (xHNO$_3$ = 0.065). The changes near 3000 cm^{-1} indicate the formation of ice in the droplets.

The concentrations were quantified by comparing the measured spectra with calculated spectra of droplets having known concentrations. The calculations assumed log-normal size distributions and used Mie theory with optical constants reported by Norman et al.[24] These optical constants were measured at 220 K, which permits their direct use at the temperatures of our experiments. Concentrations not represented in the published data set were obtained by interpolation using cubic splines, because the variation of the optical constants with concentration is very smooth.

The concentration and the log-normal size parameters, $\langle r_g \rangle$ (the geometric radius) and σ (the standard deviation), for a given experiment were all determined simultaneously in the same procedure. This involves computing a series of spectra having different $\langle r_g \rangle$, σ, and concentration values that span the range of interest and then determining the minimum χ^2 (goodness of fit) parameter between the calculated spectra and the measured spectrum using a simplex procedure. For the concentration range reported here, there were detectable changes in the minimum χ^2 for concentrations differing by more than about 0.005 mole fraction units, so the error in the concentration determination is taken to be ±0.005 mole fraction unit.

Freezing Temperatures for Nitric Acid Concentrations Lower than xHNO$_3$ $\approx$ 0.1. For the most dilute particles, freezing causes significant changes in the OH stretching region between 2600 and 3600 cm^{-1}. These can be seen in Figure 1, which gives the temperature evolution of the spectra of droplets having xHNO$_3$ = 0.065. Mie fits to the spectra of the liquid droplets (at 225 K) give log-normal parameters $\langle r_g \rangle = 2.2\ \mu$m and $\sigma = 1.3$. The changes between 2500 and 3500 cm^{-1}, which we have observed in previous studies of this kind,[25] are characteristic of ice formation.

To quantify the temperature at which H_2O ice forms in these dilute droplets, we use a procedure based on difference spectra that is similar to one used in our previous work. We subtract the measured spectrum of the liquid droplets recorded at 226 K from each subsequent spectrum. The resulting difference spectra are shown in the top panel of Figure 2. The lower panel shows the difference spectrum that results when calculated spectra of water and ice aerosols are subtracted. The optical

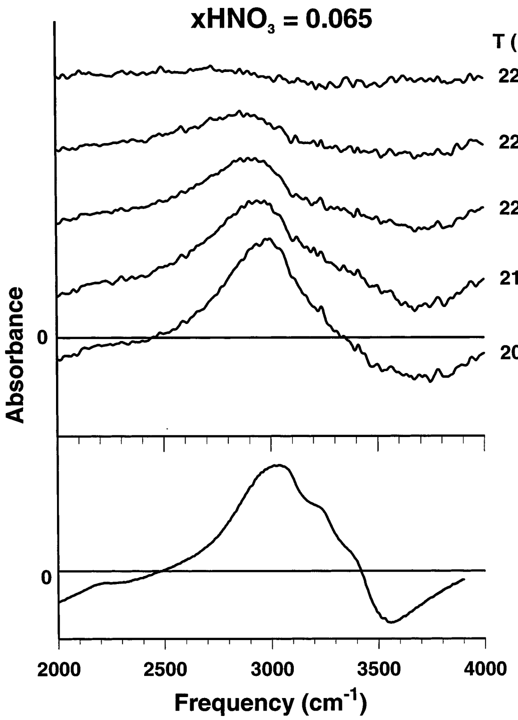

Figure 2. Difference spectra (top) obtained by subtracting the measured spectrum of liquid droplets recorded at 226 K from each spectrum shown in Figure 1 and Calculated water aerosol spectrum minus calculated ice aerosol spectrum (bottom), both having $\langle r_g \rangle = 1$ μm and $\sigma = 1.5$.

constants used in the calculations are those of Niedziela et al.[26] (ice) and Kou et al.[27] (water). This calculation was intended to illustrate the shift in extinction frequency that occurs on conversion of some of the water in a liquid droplet to ice. The spectral data do not contain enough information to extract unique size distributions and compositions for the two components, so both of the (log-normal) size distributions for the calculated spectra were taken to have $\langle r_g \rangle = 1$ μm and $\sigma = 1.5$ for the purpose of this illustration. The calculation shows that when ice appears in a water droplet, there is a strong increase in the amplitude at 3000 cm^{-1} and a corresponding decrease at 3500 cm^{-1}. The resemblance of the calculated spectrum to the lower spectrum in the top panel is evidence that ice has formed in these dilute nitric acid droplets.

The root-mean-square (rms) value of the integral over the difference spectra between 2500 and 3500 cm^{-1} is used as the measure of the amount of ice formed. The renormalized value of this integral, expressed as a percentage change from the highest temperature in the $x\text{HNO}_3 = 0.065$ experiment is shown in Figure 3. The integral rises from about 226 K and reaches a plateau at about 215 K. The fact that it reaches a plateau indicates that for this experiment the entire sample had frozen at the lowest temperature. The temperature range over which this occurs is a reflection of the width of the particle size distribution; the largest particles nucleate at the highest temperatures, followed by the smaller ones. Droplets in which a nucleus has formed will grow crystals of detectible size during their 20−30 s residence time in the crystal growth section, where the temperature is about 20 K higher than in the nucleation section. Thus the nucleation temperature, the parameter being sought, is the highest temperature at which frozen particles are first detected. To be consistent with our previous practice, we define this as the temperature at which the curve in Figure 3 rises to 10% of its final value.

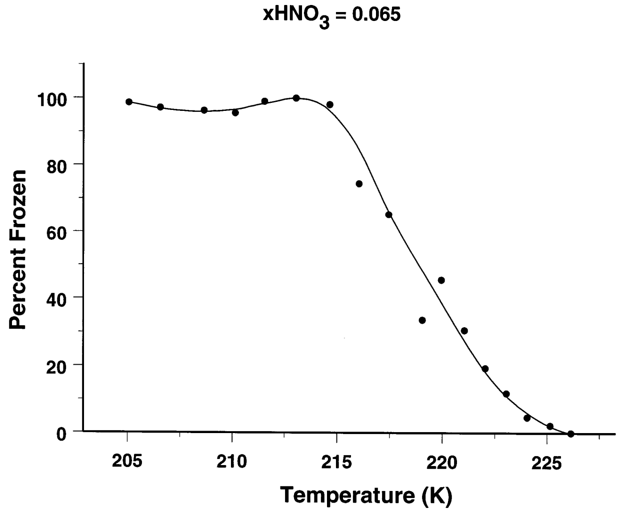

Figure 3. The rms value of the integral between 2500 and 3500 cm^{-1} over the difference spectra shown in Figure 2.

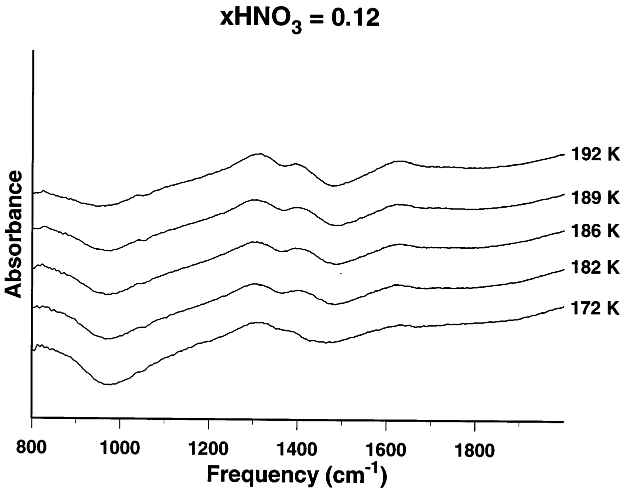

Figure 4. Changes in absorbance as a result of the freezing of aerosol particles having $x\text{HNO}_3 = 0.12$: (top) liquid droplets; (bottom) partly frozen particles.

Freezing Temperatures for Nitrate Concentrations Higher than $x\text{HNO}_3 \approx 0.1$. For particles having $x\text{HNO}_3$ in the range between about 0.1 and 0.2, significant changes occur in both the OH spectral region described above and the $\nu_3(E)$ NO_3^- band used in the determination of the concentration. The changes that occur in the NO_3^- band and how they are used to determine the amount of freezing are shown in Figures 4 and 5. Figure 4 shows the changes in the absorbance spectra during the freezing of aerosol particles having $x\text{HNO}_3 = 0.12$. The top spectrum shows liquid droplets; in the bottom one, they are partly frozen. Mie fits to the spectra of the liquid droplets (192 K) give log-normal parameters $\langle r_g \rangle = 1.4$ μm and $\sigma = 1.5$. The $\nu_3(E)$ region between 1220 and 1440 cm^{-1} is expanded in Figure 5 to demonstrate how the required information is extracted. The heavy solid curves in Figure 5a,b are the expanded views of the measured spectra at the top and bottom of Figure 4, respectively. The doublet structure of the band is evident. The three thin solid curves in each case are two Lorentzian functions and a linear baseline that were fitted to the measured spectra to quantify empirically the doublet band areas. (The baseline was necessary to account for interference from a H_2O band near 1600 cm^{-1}, which changes slightly during freezing.)

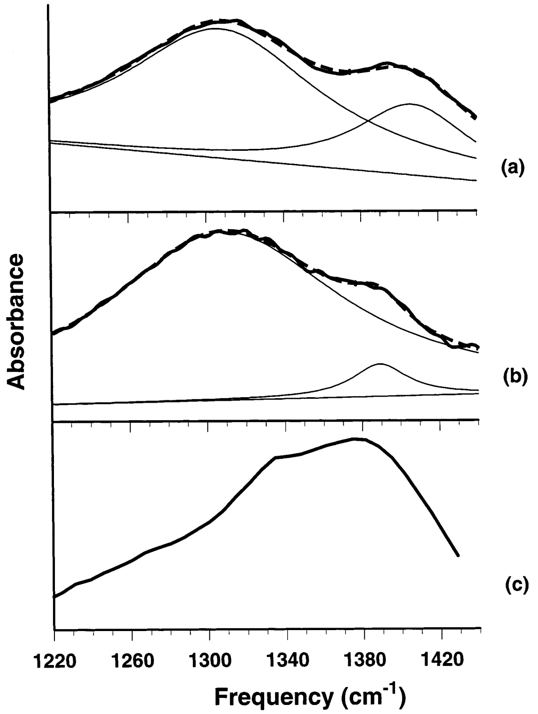

Figure 5. Expanded view of the spectral region in Figure 4 containing absorbances of the NO_3^- ion. Heavy solid curves in panels a and b are measured spectra at the top and bottom of Figure 4, respectively; that in panel c is the spectrum of pure NAT aerosol. Thin solid curves in panels a and b are Lorentzian functions and a linear baseline that were fitted to the measured spectra. Heavy dashed curves in panels a and b are the resulting fits.

In going from liquid (Figure 5a) to partly solid (Figure 5b), the left member of the doublet remains at 1310 cm^{-1} but the right member appears to move downward from 1408 to about 1390 cm^{-1}. The reason for this apparent shift may be inferred from Figure 5c, which shows the spectrum of pure NAT aerosol. The maximum absorbance of NAT lies between 1380 and 1390 cm^{-1}, and the increase in the amount of NAT with decreasing temperature causes the apparent downward shift from 1408 cm^{-1} of the right-hand member of the doublet.

To quantify the amount of NAT that forms, we developed an empirical method based on the areas of the Lorentzians fitted to the two identifiable members of the doublet. The resulting fits, which are shown as the dashed curves in Figure 5, parts a and b, respectively, agree very well with the measurements. (Only one Lorentzian was used to represent the high-frequency component of the ν_3(E) doublet and NAT because these were not spectrally resolved.) The frequencies, as well as the widths of the Lorentzians, were allowed to vary during the fitting procedure, and as expected, the low-frequency component did not move with decreasing temperature, while the high-frequency component moved downward almost to the location of the NAT maximum.

To determine the amount of NAT present, we used the fact that the NAT band is weaker than the component of the doublet that overlaps it, so the area of the right-hand Lorentzian decreases as freezing progresses. Although indirect, this gives a satisfactory measure of the phase change as illustrated in Figure 6, in which the solid circles give the area of this Lorentzian as a function of temperature. The solid curve is a weighted least-squares fit to these points. The decrease in the area with temperature between 192 and 178 K is consistent with the conversion of liquid to NAT. We designate the freezing point as the temperature at which the least-squares fit falls to 90% of its initial value.

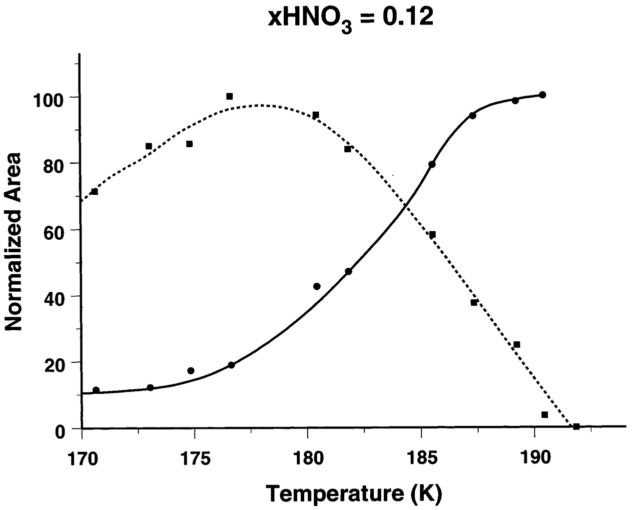

Figure 6. The area of the left-hand Lorentzian (● and solid curve) in Figure 5 as a function of temperature and rms value (■ and dashed curve) of the integral between 2500 and 3500 cm^{-1} of the differences among the spectra of Figure 4 (i.e., for $x\mathrm{HNO_3} = 0.12$), calculated in the same way as those shown in Figure 2.

In the $x\mathrm{HNO_3}$ range between 0.1 and 0.2, freezing causes abrupt and simultaneous changes in both the area of the Lorentzian indicating the formation of NAT and the area of the OH difference band that signals the formation of ice. The change in the latter for the $x\mathrm{HNO_3} = 0.12$ experiment is also shown in Figure 6 as a dashed line; the experimental points to which this is fitted are the solid squares. Both changes are large, clearly indicating that both NAT and ice are formed when the particle freezes. They do not, however, give any direct indication of which nucleates first. We will discuss this point further in a later section.

Results

Using the procedures described above, the freezing temperatures and concentrations were determined over the concentration range $0 < x\mathrm{HNO_3} < 0.2$. The results were added to those reported previously[19] to produce the complete phase diagram from $0 < x\mathrm{HNO_3} < 0.5$, which is shown in Figure 7. The triangular points show the measurements carried out in the present work. The maximum vertical and horizontal dimensions of these points give the estimated experimental uncertainties in the temperature and concentration. The two solid curves in the lower part of the figure are polynomial fits to the data sets measured in our experiments. These curves represent the kinetically constrained solid–liquid phase boundaries defined by the temperatures at which 10% of the aerosol sample has frozen. The corresponding bulk equilibrium phase diagram is shown in the upper part of the figure for comparison.

We have also included the results of Chang et al.[22] as the dashed curve extending from $x\mathrm{HNO_3} = 0$ to 0.12. While the Chang et al. curve is systematically below ours, their criterion for the freezing temperature was that 90% of the sample be frozen, and the difference between their result and ours is not unreasonable on the basis of the extent of freezing as a function of temperature shown in Figures 3 and 6.

Discussion

Figure 7 summarizes the differences between the bulk equilibrium phase diagram and the kinetically constrained

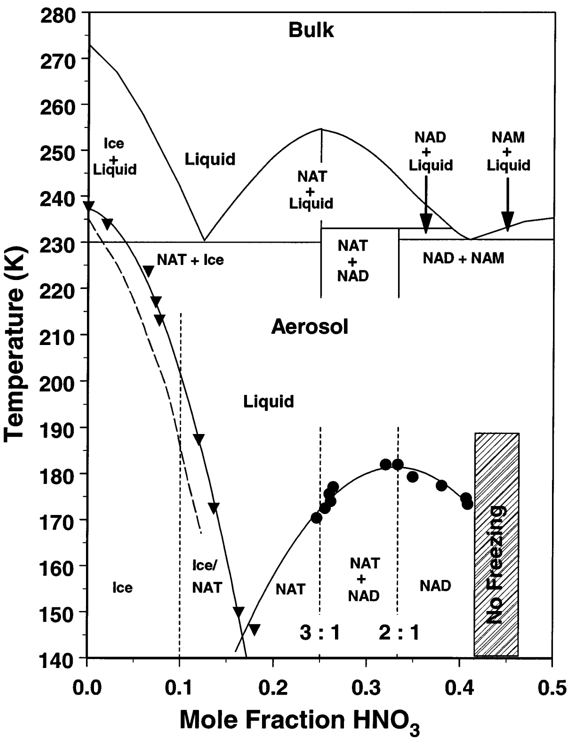

Figure 7. Solid−liquid phase boundaries for the nitric acid−water system in the concentration range $0 < xHNO_3 < 0.5$: (upper panel) equilibrium bulk phase diagram; (lower panel) kinetically constrained solid−liquid phase boundaries for a nitric acid aerosol sample giving the temperatures at which 10% of the aerosol sample has frozen in our experiment. The triangular points are measurements carried out in the present work; circles and squares are previous measurements done in our laboratory. The long dashes show the results of Chang et al.[22] See text for a description of the vertical dashed lines.

behavior characteristic of aerosol droplets. There are several significant differences. For the aerosol, the eutectic point occurs at $xHNO_3 \approx 0.17$, while for the bulk it is at $xHNO_3 = 0.125$. The highest freezing temperature for the droplets occurs at the 2:1 stoichiometry, whereas it is at a stoichiometry of 3:1 for the bulk. Also, our previous experiments showed that NAD is produced from droplets nucleated in the composition range $0.25 \leq xHNO_3 \leq 0.42$, whereas only NAT is produced from the bulk in this range.

All of these differences stem from the influence of the nucleation kinetics. Because the nucleation activation energy of NAT is higher than that of NAD over the temperature range explored here,[28] the homogeneous nucleation of NAT is inhibited at low temperatures. This conclusion is reinforced by experiments reported previously[19] that examined the effect of different temperature profiles on droplets having a 3:1 stoichiometry ($xHNO_3 = 0.25$). In one of these previous experiments, the nucleation and observation sections of the flow tube were held at the same temperature. This is a “one-stage” experiment in which the droplets are cooled rapidly and monotonically in the nucleation section and their spectrum is recorded at the same temperature in the observation section. This experiment produced a combination of NAT and NAD crystals when the temperature reached 168−170 K. In another experiment, the droplets were subjected to the same procedure except that the observation section was held at a higher temperature (188 K) to promote rapid crystal growth on the previously formed nuclei. In this “two-stage” experiment, the only crystals observed were the thermodynamically more stable form, NAT. We conclude from these two experiments that NAD nucleated in the droplets, despite the fact that their stoichiometry was 3:1, and that NAT crystals grew preferentially on the NAD nuclei.

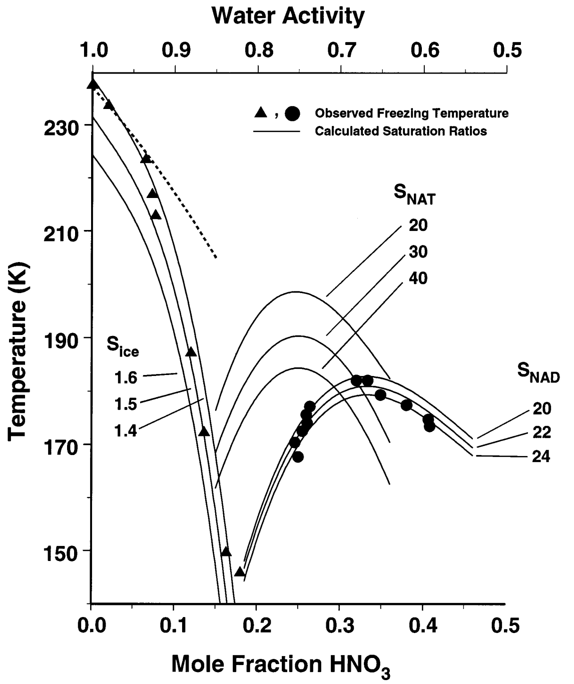

Figure 8. Selected saturation ratios (solid curves) for NAD, NAT, and ice, nucleation temperatures (points) reported in Figure 7, and the predicted ice freezing curve (dashed curve) using the criterion that only water activity determines the nucleation temperature.[29]

All of the experiments reported in this paper were carried out using a “two-stage” temperature profile in which the temperature of the observation section was held about 30 K above that of the nucleation section. Thus, the nucleation temperatures reported in Figure 7 for the concentration range $0 \leq xHNO_3 \leq 0.2$ are determined by the species having the lowest nucleation activation energy, but the crystalline solids observed are those with the most rapid crystal growth.

The vertical dashed line at $xHNO_3 \approx 0.1$ in Figure 7 separates the regions where the observed crystalline products are ice and NAT. Because only ice is observed to the left of this line, it is clear that ice nuclei form in this concentration region. Both ice and NAT are observed in the concentration region between this line and the eutectic. Despite the appearance of NAT in these spectra, we believe that the initial nucleus that forms in this region is ice. NAT would be expected to grow on these ice nuclei, because it is the most thermodynamically stable species in this part of the phase diagram.

Additional support for the contention that ice nucleates in this concentration range is given by the supersaturation curves for NAD, NAT, and ice, which are plotted as solid curves in Figure 8. The saturation ratios are indicated for each curve. The measured freezing temperatures reported in Figure 7 are reproduced here as points. All of these measured data fall along constant supersaturation ratio curves for ice and NAD but bear little resemblance to the curves for NAT. We conclude, therefore, that for the concentration range explored in this work ($0 < xHNO_3 < 0.2$) ice nucleates homogeneously in the aerosols and NAT crystals grow on the ice nuclei in the higher concentration regions.

We examined the hypothesis of Koop et al.[29] that the water activity is the only important factor in determining the temperature of homogeneous ice nucleation in solutions, without respect to the chemical identity of the solute. We compared the ice nucleation temperatures predicted by the criterion of Koop et al. with the nucleation temperatures that we measured. The predicted nucleation temperatures were determined by using the equilibrium model of Clegg et al.[30] to calculate the water activities at the equilibrium ice freezing temperatures appropriate to the conditions of our experiment for the concentration range $0 < x\mathrm{HNO_3} < 0.125$. The resulting temperature−activity curve was shifted by 0.305 activity units toward higher water activities and plotted in Figure 8 as the dashed curve. This curve is the same as the solid curve in Figure 1b of Koop et al. If our data conformed to the Koop et al. model, the measured points would fall along this curve. They do so for dilute solutions up to $x\mathrm{HNO_3} \approx 0.075$, but our measured freezing temperatures drop somewhat more quickly than the theoretical curve for higher $\mathrm{HNO_3}$ mole fractions. Thus our data indicate that the hypothesis of Koop et al. is accurate for dilute solutions but becomes progressively worse for more concentrated ones.

Atmospheric Implications. Our experimental conditions reproduce those found in the atmosphere in all respects except that of time scale, so this must be addressed before drawing atmospheric conclusions from our results. The residence time in the nucleation section of the flowtube is 21−36 s. For the purposes of this discussion, we will assume that the atmospheric time scale for PSC nucleation is 10 h.

Although large, this difference in the time scales does not affect the determination of the nucleation temperature very much because the temperature dependence of the nucleation rate constant, $J(T)$, is very strong. We approximate the temperature dependence of the rate constant using the parametrization of Koop et al.,[29] which provides a reasonable description of our measurements, as shown above. According to this, $J(T)$ changes by at least an order of magnitude per degree near the freezing temperature in the concentration range $0 < x\mathrm{HNO_3} < 0.18$, which is the range in which we find ice formation.

When homogeneous nucleation is treated as a first-order rate process, the fraction of droplets that nucleate after being held at a temperature T for a time Δt is given by the nucleation probability $P_\mathrm{N} = (1 - \exp\{-J(T)V(r)\Delta t\})$ where $V(r)$ is the droplet volume. We assumed a droplet diameter of 1 μm, corresponding to a volume of 5×10^{-13} cm^3, and plotted P_N vs temperature for the range $0 < x\mathrm{HNO_3} < 0.15$ for the two time scales. This showed that $T_{10}^{\mathrm{at}} - T_{10}^{\mathrm{ft}}$, the difference between the temperature at which 10% of the sample freezes in the atmosphere and in the flow tube, ranges from 2 K for $x\mathrm{HNO_3} = 0$ to 3.5 K for $x\mathrm{HNO_3} = 0.15$. Although the absolute values of these temperatures are too high by more than 20 K in the more concentrated region, as shown by the dashed curve in Figure 8, we believe the difference between the temperatures is probably more accurate because it depends primarily on the difference in the time scales. Thus the freezing curve for dilute nitric acid aerosols under atmospheric conditions and time scales may be approximated by adding about 3 K to the measured freezing curve shown in Figure 7.

Conclusions

We have reported the complete binary nitric acid/water phase diagram for micrometer-sized aerosol particles. Kinetic barriers have a strong effect on the nucleation and crystal growth phases during the freezing of these particles with the result that the aerosol phase diagram differs from that of the bulk material in many significant ways. These are summarized in Figure 7. These effects, in turn, influence the formation and properties of clouds in the stratosphere and upper troposphere.

Ice will nucleate homogeneously on atmospheric time scales in dilute nitric acid aerosols ($0 < x\mathrm{HNO_3} < 0.15$) at temperatures about 3 K warmer than the measured (solid) curve in the lower part of Figure 7. For the most dilute part of this range, up to about $x\mathrm{HNO_3} \approx 0.075$, the nucleation temperatures are in the range of upper tropospheric temperatures on synoptic scales where these dilute aerosols would be expected to occur. For more concentrated aerosols, the nucleation temperature drops rapidly and no homogeneous ice nucleation can be expected under synoptic upper tropospheric temperatures where $x\mathrm{HNO_3} > 0.125$.

We observe that NAT crystals grow on ice nuclei at temperatures above 185 K for $0.1 < x\mathrm{HNO_3} < 0.15$, and it is likely that this occurs for more dilute concentrations as well because NAT and ice are the thermodynamically stable components in this part of the phase diagram. This is consistent with the observation that low-temperature cirrus clouds in the upper troposphere have many of the same optical characteristics as type 1 PSCs.[31]

The most concentrated nitric acid aerosols are found in the polar stratosphere, where equilibrium models indicate that even at the lowest temperatures $x\mathrm{HNO_3}$ is rarely above about 0.2 (47 wt %). Figure 7 shows that in this higher concentration range ($0.15 < x\mathrm{HNO_3} < 0.2$) homogeneous nucleation is not possible at stratospheric temperatures.

Acknowledgment. We acknowledge many helpful discussions with Professor Allan Bertram. Financial support for this work was provided by the Natural Sciences and Engineering Research Council of Canada.

References and Notes

(1) Wooldridge, P. J.; Zhang, R.; Molina, M. J. *J. Geophys. Res., [Atmos.]* **1995**, *100*, 1389−1396.

(2) Carslaw, K. S.; Luo, B. P.; Clegg, S. L.; Peter, T.; Brimblecombe, P.; Crutzen, P. J. *Geophys. Res. Lett.* **1994**, *21*, 2479−2482.

(3) Meilinger, S. K.; Koop, T.; Luo, B. P.; Huthwelker, T.; Carslaw, K. S.; Krieger, U.; Crutzen, P. J.; Peter, Th. *Geophys. Res. Lett.* **1995**, *22*, 3031−3034.

(4) Tsias, A.; Prenni, A. J.; Carslaw, K. S.; Onasch, T. P.; Luo, B. P.; Tolbert, M. A.; Peter, T. *Geophys. Res. Lett.* **1997**, *24*, 2303−2306.

(5) Carslaw, K. S.; Peter, T.; Bacmeister, J. T.; Eckermann, S. D. *J. Geophys. Res. D: Atmos.* **1999**, *104*, 1827−1836.

(6) Deshler, T.; Peter, Th.; Müller, R.; Crutzen, P. *Geophys. Res. Lett.* **1994**, *21*, 1327−1330.

(7) Toon, O. B.; Browell, E. V.; Kinne, S.; Jordan, J. *Geophys. Res. Lett.* **1990**, *17*, 393−396.

(8) Toon, O. B.; Tabazadeh, A.; Browell, E. V.; Jordan, J. *J. Geophys. Res.*, [*Atmos.*] **2000**, *105*, 20589−20615.

(9) Browell, E. V.; Butler, C. F.; Ismail, S.; Robinette, P. A.; Carter, A. F.; Higdon, N. S.; Toon, O. B.; Schoeberl, M. R.; Tuck, A. F. *Geophys. Res. Lett.* **1990**, *17*, 385−388.

(10) Larsen, N.; Knudsen, B. M.; Rosen, J. M.; Kjome, N. T.; Neuber, R.; Kyr, E. *J. Geophys. Res.* **1997**, *102*, 23505−23517.

(11) Schneider, J.; Arnold, F.; Bürger, V.; Doste-Franke, B.; Grimm, F.; Kirchner, G.; Klemm, M.; Stiop, T.; Wohlfrom, K. H.; Siegmund, P.; van Velthoven, P. F. J. *J. Geophys. Res.* **1998**, *103*, 25337−25343.

(12) Carslaw, K. S.; Clegg, S. L.; Brimblecombe, P. *J. Phys. Chem.* **1995**, *99*, 11557−11574.

(13) Meilinger, S. K.; Tsias, A.; Dreiling, V.; Kuhn, M.; Feigl, C.; Ziereis, H.; Schlager, H.; Curtius, J.; Sierau, B.; Arnold, F.; Zoger, M.; Schiller, C.; Peter, T. *Geophys. Res. Lett.* **1999**, *26*, 2207−2210.

(14) Omar, A. H.; Gardner, C. S. *J. Geophys. Res.* **2001**, *106*, 1227−1236.

(15) Laaksonen, A.; Hienola, J.; Kulmala, M.; Arnold, F. *Geophys. Res. Lett.* **1997**, *24*, 3009−3012.

(16) Ravishankara, A. R.; Hanson, D. R. *J. Geophys. Res.*, [*Atmos.*] **1996**, *101*, 3885−3890.

(17) Salcedo, D.; Molina, L. T.; Molina, M. J. *J. Phys. Chem. A* **2001**, *105*, 1433−1439.

(18) Salcedo, D.; Molina, L. T.; Molina, M. J. *Geophys. Res. Lett.* **2000**, *27*, 193−196.

(19) Bertram, A. K.; Dickens, D. B.; Sloan, J. J. *J. Geophys. Res.*, [*Atmos.*] **2000**, *105*, 9283−9290.

(20) Bertram, A. K.; Sloan, J. J. *J. Geophys. Res.*, [*Atmos.*] **1998**, *103*, 3553−3561.

(21) Bertram, A. K.; Sloan, J. J. *J. Geophys. Res.*, [*Atmos.*] **1998**, *103*, 13261−13265.

(22) Chang, H. Y. A.; Koop, T.; Molina, L. T.; Molina, M. J. *J. Phys. Chem. A* **1999**, *103*, 2673−2679.

(23) Querry, M. R.; Tyler, I. L. *J. Phys. Chem.* **1980**, *74*, 2495−2499.

(24) Norman, M. L.; Qian, J.; Miller, R. E.; Worsnop, D. R. *J. Geophys. Res. D: Atmos.* **1999**, *104*, 30571−30584.

(25) Bertram, A. K.; Patterson, D. D.; Sloan, J. J. *J. Phys. Chem.* **1996**, *100*, 2376−2383.

(26) Niedziela, R. F.; Miller, R. E.; Worsnop, D. R. *J. Phys. Chem. A* **1998**, *102*, 6477−6484.

(27) Kou, L.; Labrie, D.; Chylek, P. *Appl. Opt.* **1993**, *32*, 3531−3540.

(28) Salcedo, D.; Molina, L. T.; Molina, M. J. *J. Phys. Chem. A* **2001**, *105*, 1433−1439.

(29) Koop, T.; Luo, B.; Tsias, A.; Peter, T. *Nature* **2000**, *406*, 611−614.

(30) Clegg, S. L.; Brimblecombe, P.; Wexler, A. S. *J. Phys. Chem. A* **1998**, *102*, 2137−2154.

(31) Omar, A. H.; Gardner, C. S. *J. Geophys. Res. D: Atmos.* **2001**, *106*, 1227−1236.